PNAS
www.pnas.org

Supplementary Information for

Optical vector field rotation and switching with near-unity transmission by fully developed chiral photonic crystals

Chun-Wei Chen and Iam Choon Khoo*

Iam Choon Khoo
Email: ick1@psu.edu

This PDF file includes:

SI Notes 1–3
Figures S1–S3
Legend for Movie S1
SI References

The other supplementary material for this manuscript is:

Movie S1

SI Note 1: Materials and Methods

Sample preparation. The cholesteric liquid crystals (CLC) used in this work consist of a multicomponent nematic host HNG741100-000 (experiments shown in Figs. 4–6) or HNG715500-000 (experiment shown in Figs. 3 and 7) and a chiral agent R5011 with different mixing ratios (all from HCCH). HNG741100-000 exhibits a nematic phase from 82°C to below −30°C and a (negative) dielectric anisotropy $\Delta\varepsilon$ of about −11 at 1 kHz, 25 °C. HNG715500-000 exhibits a nematic phase from 82°C to below –40°C; at 25 °C, $n_e \approx 1.55$, $n_o \approx 1.48$, and $\Delta\varepsilon = \varepsilon_{\parallel} - \varepsilon_{\perp} \approx 7.4 - 21.6 = -14.2$ at 1 kHz. R5011 is the common name for (13bR)-5,6-dihydro-5-(trans-4-propylcyclohexyl)-4H-dinaphtho[2,1-f:1',2'-h][1,5]dioxonin, which introduces structural chirality into the nematic host. R5011 is right-handed and exhibits twisting power $\beta > 120\ \mu m^{-1}$ in HNG741100-000. The materials were heated above the clearing point of the nematic host under magnetic stirring for one to three hours to ensure homogeneous mixing. The clearing points of the cholesteric mixtures are very close to that of the nematic host. The CLC cells were made with two indium-tin-oxide-coated glass windows spaced by adhesive plastic strips [each strip of thickness ~0.3–0.5 mm]. Prior to the assembly, the windows were pretreated with polyvinyl alcohol (Sigma-Aldrich) and rubbed unidirectionally to define the director orientation on the cell surface. The cells were filled with the cholesteric mixtures in the isotropic phase and then sealed with an epoxy adhesive QS-2 (KS Bond).

It is important to first point out here the severe limitations encountered by conventional self-assembly techniques to fabricate very thick CLCs. Molecular self-assembly without external bias field exploits the long-range orientational order imposed by the aligned and strongly anchored molecules on the cell substrate and can ensure uniformly standing helices (USH) in thin CLCs up to 10's of μm in thickness. However, the effect of surface anchoring on the bulk LC becomes weaker with increasing cell gap, and CLCs with thicknesses > 100's of μm are often amorphous and highly scattering with a dense network of oily streaks [Fig. S1*A*]. Although thin oily streaks are unstable and spontaneous grain growth can occur in time, the efficacy of forming monocrystalline CLC by field-free self-assembly is very limited as depicted in Fig. S1*A*. In the transmission spectrum captured a month after cell fabrication [Fig. S1*B*], although a photonic bandgap can be observed, it was highly distorted in the short-wavelength region.

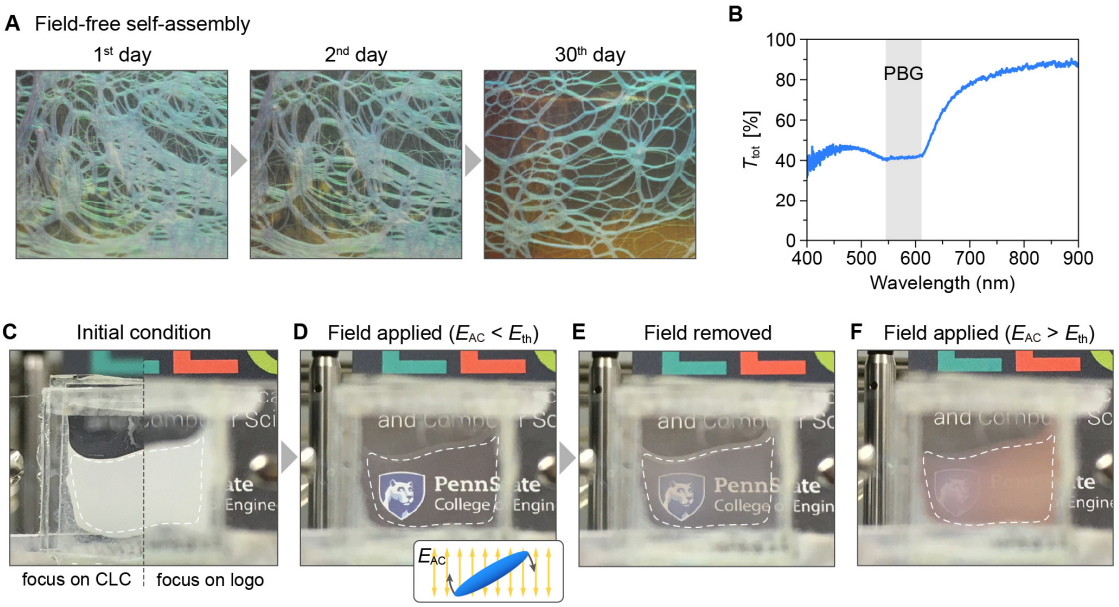

Figure S1. Upper row: (*A*) photographs of a 0.3-mm thick positive-$\Delta\varepsilon$ CLC sample taken on the 1st, 2nd, and 30th days of field-free self-assembly. Material: S5011-doped E7. (*B*) Total transmission (T_{tot}) spectrum of the sample on the 30th day. Lower row: photographs of a 0.3-mm negative-$\Delta\varepsilon$ CLC sample placed in front of Penn State logo (*C*) in the initial condition with an amorphous (focal-conic) texture, (*D*) at $E_{AC} < E_{th}$ [1 kHz] (*E*) after field removal, and (*F*) at $E_{AC} > E_{th}$ [1 kHz], where E_{th} is the threshold field strength for inducing orientational instability. Inset shows the dielectric alignment mechanism.

The situation maybe improved somewhat by using a nematic constituent with negative dielectric anisotropy $\Delta\varepsilon < 0$ and applying a field (after the self-assembly process has ensued) to enforce planar alignment of the director axis and standing helices. In that case, although the sample is initially in a highly scattering state as shown in Fig. S1*C*, the applied AC field will remove most of the oily streaks resulting in a relatively clearer sample [Fig. S1*C*,*D*]. Nevertheless, microscopic examination showed that many thick streaks (typically hundreds of microns in width) remain. Upon removal of the applied field, more oily streaks re-appeared, and the sample became more scattering [Fig. S1*E*]. These oily streaks, formed during molecular self-assembly without any stabilizing applied field, cannot be removed by simply raising the applied field strength after the self-assembly process. In fact, when the field strength exceeded a certain threshold field E_{th} (1), orientation instability began to set in; the resulting helix distortion caused the Bragg reflection band at cell normal to shift from near infrared to red and manifested as reddish reflection in Fig. S1*F*.

The strategy of the FASA technique *is to prevent the oily streaks from ever forming in the first place*. The procedure is to begin applying the bias field when the CLC mixture is still in the isotropic phase and to maintain the field as the sample cools down to below the transition temperature when molecular self-assembly process begins and to continue applying the field for a long time [~ 3 hours] after the self-assembly process is completed, as schematically depicted in Fig. 3*A* (see also Movie S1).

The sample (cell with a CLC mixture) was first heated to 10–30°C above the clearing point (~80°C) to completely randomize molecular orientations and then allowed to cool down to the final [room] temperature during which the sample underwent molecular self-assembly. An AC field was applied across the cell windows throughout the cooling period and maintained for another three hours at room temperature to ensure that the molecular assembly reached the steady state. The applied field was then switched off. Owing to the negative dielectric anisotropy of the nematic constituent, a planar alignment of the LC director axes along the plane of the cell window was continuously enforced to direct the self-assembly of the director axes into USH. The required field strength for FASA is inversely proportional to the magnitude of the dielectric anisotropy $|\Delta\varepsilon|$ and was on the order of ~1–2 V μm^{-1}; the frequency of the applied AC voltage should be sufficiently high (typically at 10^2–10^3 Hz) to avoid the electrohydrodynamic instabilities in the conduction regime (2). The electric field was provided by a high-voltage amplifier (TREK 2220) that was linked to a function generator (Agilent 33220A).

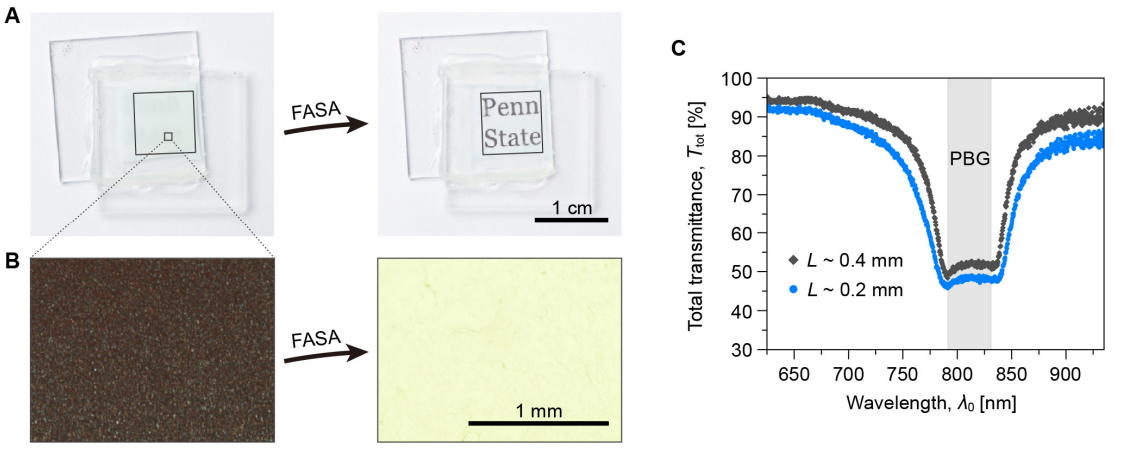

Figure S2. (*A*) Photographs of a 0.3-mm-thick cholesteric cell [placed on top of printed words] before and after the FASA treatment. (*B*) Micrographs of the 0.3-mm-thick cholesteric cell. (*C*) Total transmission spectra of 0.4 and 0.2 mm-thick samples, showing high period accuracy.

Following the FASA procedure described above, well-aligned optically clear ~mm-thick CLCs were obtained, with only a few oily streaks in the observation volume of $0.9 \times 0.7 \times 0.3$ mm^3 [Fig. S2*A*,*B*]. As can be explained by the coarse-grain model for CLC [see ref. 3], the USH configuration is extraordinarily stable in the absence of an applied field; the transmission spectra of a 400-μm-thick HN-CLC (N ~ 1700) captured when the sample was first made and 16 months after fabrication (without any post treatments) are shown to be essentially the same, despite experiencing several temperature fluctuations of ~10°C, long distance transport (Pennsylvania–Connecticut–Pennsylvania), and numerous handling during characterizations [Fig.

3*C*]. Such stability and robustness are also borne out by the consistent reproducibility of the experimental data/results on polarization rotation measurements detailed in the main text. Typically, the available cross-section for polarization rotation and other optical functions of the fabricated high-N CLC is ~1 cm^2 and can be scaled up if situation arises. It is important to note here that in thick HN-CLCs, the fabrication accuracy and spatial uniformity of the grating periods are much easier to control than their thin (μm-thick) counterparts and commercial Bragg mirrors. Commercial Bragg mirrors are fabricated by thin-film deposition and require strict thickness control at each dielectric layer—a costly and time-consuming process. By contrast, the fabrication of CLCs relies on self-assembly, which naturally evolves to a state of uniformly distributed grating periods. On the fabrication accuracy, although the natural helical pitch ($p_n = 2\Lambda_n$) of a cholesteric mixture is easily controlled by the chiral fraction (w), the fabricated CLC period in a thin cell often deviates from p_n. This is because the fabricated grating spacing Λ (= p/2) is usually elongated/compressed to comply with the fixed cell thickness and boundary alignment directions; for instance, given parallel alignment directions at the two substrates, the CLC structure should satisfy $N = L/\Lambda$ being an integer. For the same reason, spatial variations of the grating period $\Delta\Lambda$ occur because of gap nonuniformity ΔL (*i.e.*, $\Delta\Lambda = \Delta L/N$). While such nonuniformity poses serious issues in conventional thin low-N CLCs, its influence becomes negligible in very thick CLCs where N is a very large number; As clearly shown in Fig. S2*C*, the short- and long-wavelength edges of the PBGs of two samples with different thicknesses (~0.2 and ~0.4 mm) are remarkably well-matched.

Optical characterization and Polarization rotation measurement. The continuous-wave transmission spectra were measured with an incoherent white light source (Ocean Optics LS-1 tungsten halogen lamp) and a grating spectrometer (Ocean Optics Flame); Glan-Taylor calcite polarizers (Thorlabs GT10) and thin film polarizers (API AP42-008T-PSA) were used to obtain the polarized spectra. The pictures were captured using digital single-lens reflex camera (Nikon D7000 with AF-S VR Micro-Nikkor 105mm f/2.8G IF-ED). The polarized optical micrographs were obtained with microscope Eclipse LV100 POL (Nikon) and charge-coupled device DS-Fi1 (Nikon). To demonstrate giant optical rotation of complex vector fields, a He–Ne laser at 633 nm (Melles Griot 05-LHP-151), a charge-coupled device (AmScope), and two types of linear-to-cylindrical polarization converters were used. In the $|+1\rangle$ experiment, the converter was a 5-μm-thick sandwich cell containing nematic liquid crystal E7. The cell windows were pretreated with a Brilliant Yellow (azo-dye) coating, and then the photoalignment technique described in ref. 4 was applied to the azo-dye coatings to enable unidirectional and azimuthal alignments on the entrance and exit window surfaces, respectively. In the $|\pm2\rangle$ experiment, the converter was a 14-μm-thick sandwich cell containing HNG741100-000. The cell windows were pretreated with cetyltrimethylammonium bromide to induce vertical alignment in the absence of an electric field. Upon field application (above the Fréedericksz transition threshold), the LC bends down, and randomly distributed defects of topological charges +1 and –1 were generated. A linearly polarized laser beam can be converted from the linear-polarization mode to a $|\pm2\rangle$ cylindrical-polarization mode by a ±1 LC defect (5). The applied voltage was set to ~2.6 V at 1 kHz to enable half-wave conversion. In the ultrafast characterization, the linearly polarized sub-ps pulses were emitted from a Ti:Sapphire-laser-seeded optical parametric oscillator with repetition rate of 80 MHz (Coherent Chameleon), analyzed by the Glan-Taylor calcite polarizer, and detected by a grating spectrometer (Horiba iHR320). In the polarization-switching demonstration, the HN-CPC sample was mounted on a hot stage (LTS350, Linkam) connected to a temperature controller (TMS94, Linkam), and the cooling and heating rates were both set to 5°C/min.

SI Note 2: Optical properties of CPC with finite number of periods

Here we derive the expressions for the transmission, reflection, ORP, and DOS of CPC with finite N through the coupled mode analysis [Eq. 1].

Transmission and reflection. We first follow Chandrasekhar *et al.*'s formalism (6,7) to obtain the transmission and reflection coefficients. Reorganizing Eq. 1, the forward [superscript (f)] and backward [superscript (b)] propagating waves at the j^{th} lamellar plane are related to their counterparts at the neighboring planes as

$$E_{j+1}^{(\mathrm{f})} + E_{j-1}^{(\mathrm{f})} = \eta E_j^{(\mathrm{f})} \quad [S1]$$

and

$$E_{j+1}^{(\mathrm{b})} + E_{j-1}^{(\mathrm{b})} = \eta E_j^{(\mathrm{b})}. \quad [S2]$$

where

$$\eta = exp(i\delta) + exp(-i\delta) + Q^2 exp(-i\delta). \quad [S3]$$

The CPC comprises $M = N/2$ cholesteric lamellae, and no incident waves from the other side of the CPC [*i.e.*, $E_M^{(\mathrm{b})} = 0$ at $j = M$]. The reflected wave from the entrance plane ($j = 0$) is related to the backward-propagating wave at the $(M-1)^{\text{th}}$ plane as

$$E_0^{(\mathrm{b})} = f_M(\eta) E_{M-1}^{(\mathrm{b})}, \quad [S4]$$

where

$$f_M = \left[\eta^{M-1} - \frac{M-2}{1!}\eta^{M-3} + \frac{(M-4)(M-3)}{2!}\eta^{M-5} - \cdots\right]. \quad [S5]$$

Similarly, the forward-propagating waves at the entrance and exit planes are related as

$$E_0^{(\mathrm{f})} = [f_M \exp(i\delta) - f_{M-1}] E_M^{(\mathrm{f})}. \quad [S6]$$

From Eq. 1, the $E_{M-1}^{(\mathrm{b})}$ and $E_M^{(\mathrm{f})}$ are related as

$$E_{M-1}^{(\mathrm{b})} = -iQ \exp(i\delta)\, E_M^{(\mathrm{f})}. \quad [S7]$$

The σ_+-polarized reflection coefficient of a CPC is thus

$$r_+ = \frac{E_0^{(\mathrm{b})}}{E_0^{(\mathrm{f})}} = \frac{-iQ f_M \exp(i\delta)}{f_M \exp(i\delta) - f_{M-1}}. \quad [S8]$$

By assuming that the solution to Eq. S1 is in the form

$$E_{j+1}^{(\mathrm{f})} = \chi E_j^{(\mathrm{f})} \quad [S9]$$

and using the relation $\delta = 2\pi + \varepsilon$, we obtain

$$\chi + \chi^{-1} = \eta = \exp(i\varepsilon) + \exp(-i\varepsilon) + Q^2 \exp(-i\varepsilon). \quad [S10]$$

In the Bragg regime,

$$\chi = \exp\left(-2\pi \mp \sqrt{Q^2 - \varepsilon^2}\right) = \exp\left(\mp\sqrt{Q^2 - \varepsilon^2}\right) \quad [S11]$$

(– for $\lambda_0 < \lambda_{\text{mid}}$ and + for $\lambda_0 > \lambda_{\text{mid}}$).

Therefore, according to Eq. S10,

$$\eta \cong \exp\left(-\sqrt{Q^2 - \varepsilon^2}\right) + \exp\left(+\sqrt{Q^2 - \varepsilon^2}\right) = 2\cosh\left(\sqrt{Q^2 - \varepsilon^2}\right). \quad [S12]$$

Equation S5 becomes

$$f_M = \frac{\sinh\left(M\sqrt{Q^2-\varepsilon^2}\right)}{\sinh\left(\sqrt{Q^2-\varepsilon^2}\right)}. \quad [S13]$$

Similarly, from Eqs. 1 and S9,

$$E_{j+1}^{(\mathrm{b})} = \frac{\chi - \exp(-i\delta)}{\chi \exp(-i\delta) - Q^2 \exp(-2i\delta) - \exp(-2i\delta)} E_j^{(\mathrm{b})} = \chi E_j^{(\mathrm{b})}. \quad [S14]$$

Equation S8 can be rewritten as

$$r_+ = \frac{-iQ \exp(i\varepsilon)}{i\varepsilon \pm \sqrt{Q^2-\varepsilon^2}\coth\left(\frac{1}{2}N\sqrt{Q^2-\varepsilon^2}\right)}; \quad [S15]$$

note that $M = N/2$ and $Q \approx [\pi(n_e - n_o)/n_{avg}]\sin(\varepsilon)/\varepsilon$. For an N-period CPC, the σ_+-polarized reflectance is

$$R_+ = \frac{Q^2}{\varepsilon^2 + (Q^2 - \varepsilon^2)\coth^2\left(\frac{1}{2}N\sqrt{Q^2-\varepsilon^2}\right)}. \quad [S16]$$

Similarly, from Eqs. S6 and S13, the σ_+-polarized transmission coefficient is given by

$$t_+ = \frac{E_M^{(f)}}{E_0^{(f)}} = \frac{\sinh\left(\sqrt{Q^2-\varepsilon^2}\right)}{\exp(i\varepsilon)\sinh\left(\frac{1}{2}N\sqrt{Q^2-\varepsilon^2}\right) - \sinh\left[\left(\frac{1}{2}N-1\right)\sqrt{Q^2-\varepsilon^2}\right]} = \frac{\sqrt{Q^2-\varepsilon^2}\,\mathrm{csch}\left(\frac{1}{2}N\sqrt{Q^2-\varepsilon^2}\right)}{i\varepsilon + \sqrt{Q^2-\varepsilon^2}\coth\left(\frac{1}{2}N\sqrt{Q^2-\varepsilon^2}\right)}, \quad [S17]$$

and the σ_+-polarized transmittance is

$$T_+ = t_+ t_+^* = 1 - R_+. \quad [S18]$$

Optical rotatory power. The transmission coefficient can also be expressed as

$$t_+ = A\exp\left[-\frac{1}{2}iN(2\pi + \psi)\right] = A\exp\left[-\frac{1}{2}iN\psi\right], \quad [S19]$$

where A is the amplitude of the optical electric field, $\delta_+ = 2\pi + \psi$ is the accumulated σ_+ phase per lamella in the presence of the chiral Bragg resonance (CBR), and

$$\psi = \frac{2}{N}\tan^{-1}\left[\frac{\varepsilon}{\pm\sqrt{Q^2-\varepsilon^2}\coth\left(\frac{1}{2}N\sqrt{Q^2-\varepsilon^2}\right)}\right] + \frac{2\mathrm{m}\pi}{N} \quad [3]$$

(m = 0, 1, 2, ...). To compute the optical rotatory dispersions displayed in Fig. 2, we divide each spectrum into short- and long-wavelength portions with respect to the mid gap (λ_{mid}). In the MATLAB code, we define $\psi = 2(\Delta_\psi + \mathrm{m}\pi)/N$ and $\Delta_\psi = \tan^{-1}(\varepsilon/(Q^2 - \varepsilon^2)^{1/2}\coth[N(Q^2 - \varepsilon^2)^{1/2}/2])$, because the inverse tangent function is constrained to the interval $[-\pi/2, \pi/2]$. The computation starts from $\lambda_0 = \lambda_{mid}$ and m = 0; say, the current step of computation is z, m(z) = m(z – 1) + 1 whenever $|\Delta_\psi(\lambda_0) + \Delta_\psi(\mathrm{z}-1)| < |\Delta_\psi(\mathrm{z}-1)|$. The optical rotation per lamella is

$$\Delta\varphi|_{L=2\Lambda} = \frac{1}{2}(\delta_- - \delta_+) = \frac{1}{2}[\delta_- - (2\pi + \psi)], \quad [S20]$$

where $\delta_- = 2\pi p n_-/\lambda_0$ is the accumulated phase of σ_--polarized light per lamella. Equation S20 can also be written as

$$\Delta\varphi|_{L=2\Lambda} = \frac{1}{2}(\delta_- - \delta + \varepsilon - \psi) \quad [S21]$$

(note that $\Lambda = p/2$). The first two terms in the bracket on the right-hand side of Eq. S21, $\delta_- - \delta$, is the *intrinsic* phase retardation per lamella between the two circularly polarized components, which gives rise to the adiabatic rotation (AR). The latter two terms in the bracket on the right-hand side of Eq. S21 is the circular phase retardation contributed by the CBR. According to refs. 7 and 8, the AR contribution to the rotation is,

$$\Delta\varphi|^{AR}_{L=2\Lambda} = \frac{1}{2}(\delta_- - \delta) = \frac{\pi\Lambda^2(n_e - n_o)^2}{\lambda_0^2}. \quad [S22]$$

The ORP ($\Delta\varphi$ per unit length) is thus

$$\mathrm{ORP} = \frac{\pi\Lambda(n_e - n_o)^2}{2\lambda_0^2} + \frac{\varepsilon - \psi}{4\Lambda}. \quad [2]$$

Density of states. The optical DOS (D in the following formulae) is the inverse slope of the dispersion relation (9):

$$D \equiv \frac{\mathrm{d}k}{\mathrm{d}\omega} = \frac{1}{v_g}. \quad [S23]$$

For σ_--polarized light, D_- is simply $n_{avg}/c \approx (n_e + n_o)/2c$, where c is the speed of light in vacuum. To calculate the DOS for σ_+-polarized light (D_+), we first write down the dispersion relation as

$$\tan[2N\Lambda k_+(\omega)] = \frac{\mathrm{Im}[t_+(\omega)]}{\mathrm{Re}[t_+(\omega)]}. \quad [S24]$$

Let $t_+ = a + ib$. By taking the derivative with respect to ω (denoted by the Lagrange's notation), Eq. S24 becomes

$$2\Lambda k_+' \sec^2(2N\Lambda k_+) = \frac{2}{N}\frac{ab' - a'b}{a^2}. \quad [S25]$$

Since

$$\sec^2(2N\Lambda k_+) = \tan^2(2N\Lambda k_+) + 1 = \left(\frac{b}{a}\right)^2 + 1, \quad \text{[S26]}$$

D_+ is related to t_+ as

$$D_+ = \frac{1}{N\Lambda}\frac{ab' - a'b}{a^2 + b^2}. \quad \text{[S27]}$$

The relative density of states (or sometimes called the slow-down factor) is defined as the ratio between D_+'s with and without enhancement by CBR,

$$D_r = \frac{cD_+}{n_{avg}}. \quad \text{[S28]}$$

For numerical plots, it is convenient to write derivatives in terms of λ_0 as

$$a'(\omega) = \frac{-\lambda_0^2}{2\pi c} a'(\lambda_0). \quad \text{[S29]}$$

and same for b'.

Some simulations on the dependency of ORP on the unit cell number N are summarized here. As shown in Fig. S3*A*, the optical rotatory power is enhanced by the chiral Bragg resonances (peaks marked with red triangles) on the short- and long-wavelength sides of the bandgap; the magnitude of the maximum ORP grows with N because of the increased confinement of the σ_+ light in the CPC, as also evident in the density of states (DOS) curves. Figure S3*B* traces the evolutions of ORP's at three selected λ_0's, one at and two away from the short-wavelength edge (SWE): λ_{SWE} (~790 nm), 750 nm ($\lambda_{SWE} - \lambda_0 \approx 40$ nm), and 675 nm ($\lambda_{SWE} - \lambda_0 \approx 120$ nm). The maximum ORP for each N-value occurs at λ_{SWE} (~790 nm); it increases steeply as a function of N, begins to assume a more gradual ascent for $N >$ ~100, and ultimately tapers off to the saturation value corresponding to the maximum ORP ~ $\pi(n_e - n_o)/2\lambda_{SWE}$ ~ 8000°/mm. On the other hand, the other two that are detuned from the SWE exhibit amplitude oscillations and eventually saturate at lower quasi-steady-state [small-oscillation] values for $N >$ ~500. The inset shows these dependencies of the optical rotatory dispersion from $N = 20$ to $N = 500$ at an expanded wavelength scale near the SWE.

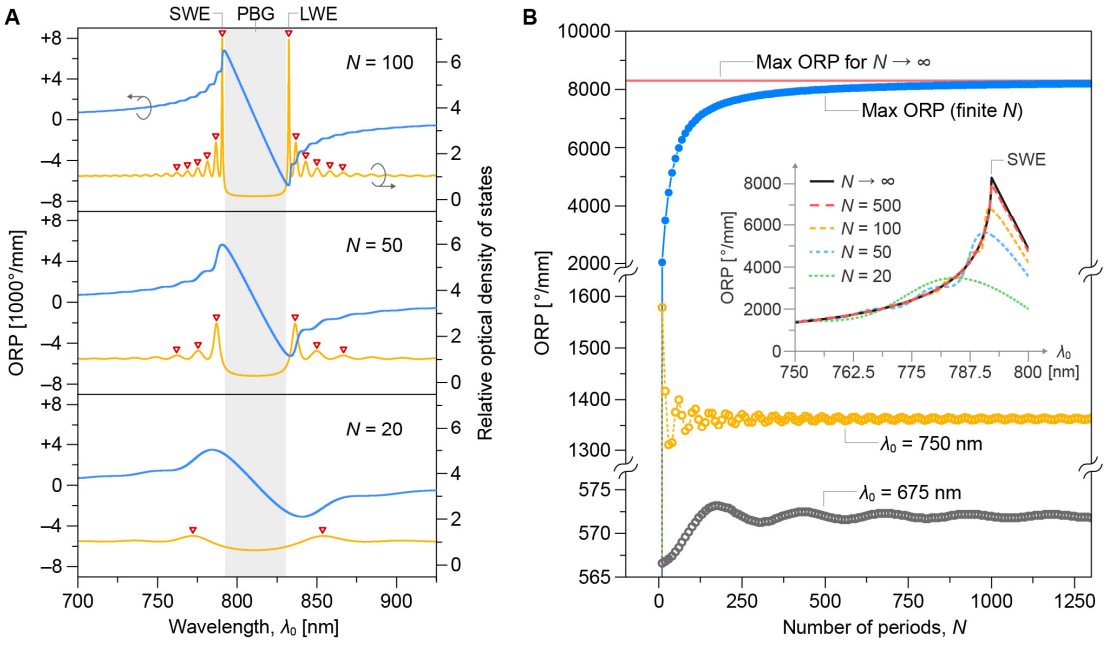

Figure S3. (*A*) Optical rotatory power (ORP) and relative photon density of states of CPCs with different period numbers (N). SWE/LWE: short-/long-wavelength edge. (*B*) Evolutions of maximum ORP, ORP at 750 nm, and ORP at 675 nm with N. Inset compares the optical rotatory dispersions of ideal CPC [$N \to \infty$] and CPCs with finite period numbers in the SWE regime.

SI Note 3: Optical properties of CPC with period number approaching infinity

From Eqs. 1, S11, and S14 (6,7),

$$r_+ = \frac{E_0^{(\mathrm{b})}}{E_0^{(\mathrm{f})}} = \frac{-iQ}{1-\exp\left[-i\left(\varepsilon \pm \sqrt{\varepsilon^2-Q^2}\right)\right]} = \frac{-Q}{\varepsilon \mp \sqrt{Q^2-\varepsilon^2}} \quad [S30]$$

(– for $\lambda_0 < \lambda_{\mathrm{mid}}$ and + for $\lambda_0 > \lambda_{\mathrm{mid}}$). The circular Bragg reflectance is thus

$$R_+ = r_+ r_+^* = \left|\frac{Q}{\pm\sqrt{Q^2-\varepsilon^2}-\varepsilon}\right|^2 \text{ outside the PBG} \quad [S31]$$

and $R_+ = 1$ within the PBG. At the limit, $\psi = (\varepsilon^2 - Q^2)^{1/2}$, and so Eq. 2 can be reduced to Eq. 4:

$$\mathrm{ORP} = \frac{\pi\Lambda(n_\mathrm{e}-n_\mathrm{o})^2}{2\lambda_0^2} + \frac{\varepsilon-\sqrt{\varepsilon^2-Q^2}}{4\Lambda} = \frac{\pi\Lambda(n_\mathrm{e}-n_\mathrm{o})^2}{2\lambda_0^2} + \frac{\pi(\lambda_\mathrm{mid}-\lambda_0)}{2\Lambda\lambda_0}\left(1-\sqrt{1-\frac{Q^2}{\varepsilon^2}}\right). \quad [S32]$$

The σ_+ dispersion relation is (10)

$$k_+ = \frac{2\pi \pm i\sqrt{Q^2-\varepsilon^2}}{2\Lambda} \quad [S33]$$

(– for $\lambda_0 < \lambda_{\mathrm{mid}}$ and + for $\lambda_0 > \lambda_{\mathrm{mid}}$), and the σ_- dispersion relation is $k_- = 2\pi n_{\mathrm{avg}}/\lambda_0 + \pi(n_\mathrm{e} - n_\mathrm{o})^2/2\lambda_0^2$; $k_- \approx 2\pi n_{\mathrm{avg}}/\lambda_0$ in the regime of interest.

Movie S1 (separate file). Field-assisted self-assembly (FASA) process of a sub-mm-thick CLC cell — from a transparent isotropic liquid through the highly scattering isotropic–cholesteric transition stage to the final transparent state with uniform standing cholesteric helices.

SI References

1. C.-W. Chen, A. N. Brigeman, T.-J. Ho, & I. C. Khoo, Normally transparent smart window based on electrically induced instability in dielectrically negative cholesteric liquid crystal. *Opt. Mater. Express* **8**(3), 691–697 (2018).
2. F. Carbone, L. Sorriso-Valvo, C. Versace, G. Strangi, & R. Bartolino, Anisotropy of Spatiotemporal Decorrelation in Electrohydrodynamic Turbulence. *Phys. Rev. Lett.* **106**(11), 114502 (2011).
3. O. D. Lavrentovich & D. K. Yang, Cholesteric cellular patterns with electric-field-controlled line tension. *Phys. Rev. E* **57**(6), R6269–R6272 (1998).
4. Y.-Y. Tzeng, S.-W. Ke, C.-L. Ting, A. Y. G. Fuh, & T.-H. Lin, Axially symmetric polarization converters based on photo-aligned liquid crystal films. *Opt. Express* **16**(6), 3768–3775 (2008).
5. E. Brasselet & C. Loussert, Electrically controlled topological defects in liquid crystals as tunable spin-orbit encoders for photons. *Opt. Lett.* **36**(5), 719–721 (2011).
6. S. Chandrasekhar & J. S. Prasad, Theory of Rotatory Dispersion of Cholesteric Liquid Crystals. *Mol. Cryst. Liq. Cryst.* **14**(1-2), 115–128 (1971).
7. S. Chandrasekhar & K. S. Rao, Optical rotatory power of liquid crystals. *Acta Crystallogr. Sec. A* **24**(4), 445–451 (1968).
8. H. de Vries, Rotatory power and other optical properties of certain liquid crystals. *Acta Crystallogr.* **4**(3), 219–226 (1951).
9. J. M. Bendickson, J. P. Dowling, & M. Scalora, Analytic expressions for the electromagnetic mode density in finite, one-dimensional, photonic band-gap structures. *Phys. Rev. E* **53**(4), 4107–4121 (1996).
10. S. Chandrasekhar, G. Ranganath, & K. Suresh, Dynamical theory of reflexion from cholesteric liquid crystals. *Pramana, Suppl.* **1**, 341–352 (1975).